



Published in final edited form as:

Ann Biomed Eng. 2020 April ; 48(4): 1256–1270. doi:10.1007/s10439-020-02447-7.

In vivo modulation of the blood-brain barrier permeability by transcranial direct current stimulation (tDCS)

Da Wi Shin, Jie Fan, Eric Luu, Wasem Khalid, Yifan Xia, Niranjana Khadka, Marom Bikson, Bingmei M. Fu*

Department of Biomedical Engineering, The City College of the City University of New York, New York, NY 10031

Abstract

tDCS has been used to treat various brain disorders and its mechanism of action (MoA) was found to be neuronal polarization. Since the blood-brain barrier (BBB) tightly regulates the neuronal microenvironment, we hypothesized that another MoA of tDCS is direct vascular activation by modulating the BBB structures to increase its permeability (P). To test this hypothesis, we used high resolution multiphoton microscopy to determine P of the cerebral microvessels in rat brain. We found that 20 min 0.1–1 mA tDCS transiently increases P to a small solute, sodium fluorescein (MW 376) and to a large solute, Dextran-70k, with a much higher increase in P to the large solute. By pretreating the vessel with a nitric oxide synthase (NOS) inhibitor, we revealed that the tDCS-induced increase in P is NO dependent. A transport model for the BBB was further employed to predict the structural changes by the tDCS. Comparing model predictions with the measured data suggests that tDCS increases P by temporarily disrupting the structural components forming the paracellular pathway of the BBB. That the transient and reversible increase in the BBB permeability also suggests new applications of tDCS such as a non-invasive approach for brain drug delivery through the BBB.

Keywords

multiphoton microscopy; non-invasive; nitric oxide synthase (NOS) inhibition; NG-monomethyl-L-arginine (L-NMMA); structural mechanisms; transport model across the blood-brain barrier; rat

INTRODUCTION

Transcranial direct current stimulation (tDCS) is a non-invasive electrical stimulation investigated to treat a broad range of brain disorders and to enhance memory and cognition in healthy individuals^{6, 7}. The diversity of tDCS applications is rationalized by tDCS “priming” neuronal capacity²⁰ thereby enhancing adjunctive interventions (e.g. cognitive behavioral therapy, neurorehabilitation) and the ability to learn an associated task⁵. Therefore, explaining the mechanism of action (MoA) of tDCS depends on identifying a cellular target that broadly increases brain functional capacity which historically focused on

*Corresponding author: Bingmei M. Fu, Ph.D., Department of Biomedical Engineering, The City College of the City University of New York, 160 Convent Ave, New York, NY 10031, New York, NY 10031, U.S.A., Phone: 212-650-7531; Fax: 212-650-6727, fu@ccny.cuny.edu.

neuronal polarization, although the brain endogenous process of priming neuronal capacity has been found to enhance regional blood flow in humans^{28, 31} and in animals²², as well as to increase blood nitric oxide (NO) levels¹⁹.

The wall of the cerebral microvessel is specified as the blood-brain barrier (BBB). To serve as a protecting barrier, the BBB consists of endothelial cells (ECs) with tight junctions in between ECs, which are additionally wrapped by the basement membrane (BM), pericytes and astrocyte foot processes¹². Direct effects of electrical stimulation on endothelial cells (ECs) are known, including re-orientation and secretion of vascular endothelial growth factors (VEGFs)⁴ and NO³⁰. A recent study showed that DCS can modulate water permeability of an in vitro BBB model through electroosmosis⁹. Because the BBB tightly regulates the neuronal microenvironment by maintaining proper ion concentrations for the neurons, supplying nutrients and oxygen to and removing metabolic wastes from the brain tissue, could a MoA of tDCS be direct vascular activation? Thus, the first objective of this study is to test the hypothesis that tDCS directly modulates the BBB to transiently increase its permeability. To this end, we employed our recently developed multiphoton microscopic imaging method²⁶ to quantify the BBB solute permeability of individual microvessels in rat brain following tDCS. To further investigate the cellular mechanism by which tDCS modulates the BBB permeability, the second objective of this study is to test the hypothesis that tDCS-induced increase in the BBB permeability is nitric oxide (NO) dependent. To do this, we pretreated the cerebral microvessels with a nitric oxide synthase (NOS) inhibitor, NG-monomethyl-L-arginine (L-NMMA), before measuring BBB responses to tDCS treatment.

The ultimate determinants of the BBB permeability are the structural components forming the BBB. Our previous mathematical model¹⁷ indicates that the BBB permeability to water and hydrophilic solutes is determined by the structural components in the paracellular pathway of the BBB, i.e., endothelial surface glycocalyx (ESG) of endothelial cells (ECs), interendothelial cleft, the junctions between adjacent ECs, the surrounding basement membrane (BM), pericytes and astrocytes, and the gap between astrocyte foot processes. Based on the ultrastructural parameters obtained from electron microscopy^{1, 12, 25}, this model successfully explained the measured BBB permeability to water and solutes under control conditions^{15, 32}. Therefore, the third objective of this study is to use this model to predict possible ultra-structural changes underlying transient BBB permeability enhancement by the tDCS. These transient and nano-meter scaled changes cannot be determined by any currently available experimental techniques.

Taken together, our results provide cellular and BBB ultra-structural changes that support a framework for tDCS modulated neuronal capacity through vascular activation. As considered in the discussion these findings support a vascular MoA that can complement direct neuronal polarization and suggest new applications of tDCS such as a non-invasive and selective approach for the systemic brain drug delivery through the BBB.

MATERIALS AND METHODS

Animal preparation

Adult female Sprague Dawley rats (250–300 g, age 3–4 months; Hilltop Laboratory Animals Inc., Scottsdale, PA, USA) were used to conduct the experiments. All procedures and the animals use were approved by the Institutional Animal Care and Use Committee of the City College of New York. Rats were anesthetized with pentobarbital sodium injected subcutaneously. The initial dosage was 65 mg/kg per bodyweight, and additional 3 mg/dose was given as needed. A heating pad was used to keep the rat at its body temperature throughout the entire experiment. The depth of anesthesia was monitored for the absence of withdrawal reflex to toe pinch and absence of blink reflex. Anesthesia was further checked every 15 min during the experiment; an additional 3 mg/dose pentobarbital was given when needed. At the end of the experiments, an overdose of pentobarbital (> 100 mg/kg) was administered intravenously to euthanize the animal.

The preparation of the rat skull observation area was the same as that previously described in^{26, 32}. Briefly, after a rat was anesthetized, the skull in the region of interest was exposed by shaving off the hair and cutting away the skin and connective tissue. A section of the right or left frontoparietal bone (~4 mm × 6 mm) (Fig. 1A) was carefully ground with a high-speed micro-grinder (0–50,000 rpm, DLT 50KBU; Brasseler USA, Savannah, GA, USA) until a part of it (~2 mm × 2 mm) became soft and translucent. During the process, artificial CSF (ACSF) at the room temperature was applied to the surface of the skull to dispel the heat due to grinding. After grinding, the right or left carotid artery was cannulated with PE50 tubing. The rat was then placed on a stereotaxic alignment system (SAS 597; David Kopf Instruments, Tujunga, CA, USA), and its head was fixed with two ear bars and a mouth clamp. After tDCS treatment, the cerebral microvessels were observed under the objective lens of a multiphoton microscope through the thinned part of the skull and the BBB permeability was determined. A single rat can only be used for one experimental condition and 1–3 vessels can be collected per rat for the permeability measurement.

Solutions and fluorescent test solutes

Mammalian Ringer's solution—Mammalian Ringer's solution was used for all perfusates, which was composed of (in mM) NaCl 132, KCl 4.6, MgSO₄ 1.2, CaCl₂ 2.0, NaHCO₃ 5.0, glucose 5.5, and HEPES 20. The pH was buffered to 7.40–7.45 by adjusting the ratio of HEPES acid to base. In addition, the fluorescent dye solution contained 10 mg/mL BSA (A4378; Sigma-Aldrich, USA)³². The solutions were made fresh on the day of use to avoid binding to the serum albumin.

Artificial Cerebrospinal Fluid (ACSF)—The ACSF solution composition was (in mM) NaCl 110.5, KCl 4.7, CaCl₂ 2.5, KH₂PO₄ 1.1, MgSO₄·7H₂O 1.25, NaHCO₃ 25, and HEPES 15³² and the solution was buffered to pH 7.4 ± 0.5. All chemicals were purchased from Sigma-Aldrich (USA).

Sodium fluorescein and FITC-dextran-70k—Sodium fluorescein (F6377, Sigma-Aldrich; mol. wt. 376 Da, Stokes–Einstein radius ~0.45 nm) was dissolved at 0.1 mg/mL in

the Ringer solution containing 10 mg/mL BSA. FITC-dextran-70kD (FD70s, Sigma-Aldrich; mol. wt. 70,000 Da, Stokes radius ~3.6 nm) was at the concentration of 1 mg/mL in the Ringer solution containing 10 mg/mL BSA.

L-NMMA—^NG-monomethyl-L-arginine (L-NMMA) was purchased from Sigma-Aldrich. For L-NMMA pretreatment, 1 ml of 21 mM L-NMMA was injected into the rat tail vein. This generated the initial blood L-NMMA concentration of ~1 mM if the blood volume was ~20 mL for the rats used³⁴. In the dye solution injected into the carotid artery, the concentration of L-NMMA was 0.1 mM.

To avoid hypoxia due to replacing the blood with the injected solutions, all the solutions were oxygenated by bubbling with the compressed gas composed of 95% oxygen and 5% carbon dioxide (Airgas, Bethlehem, PA, USA) for ~10 min before injection into the cerebral circulation.

Two-photon microscopy and image collection

The microvessels were observed with a 40x lens (water immersion, NA 0.8; Olympus Corporation, Tokyo, Japan), and the 12-bit images were collected by a two-photon microscopic system (Ultima, Prairie Technologies Inc., Middleton, WI, USA). For both solutes, the excitation wavelength of the two-photon microscope was set to 820 nm to clearly visualize the cerebral microvessels ~100–200 μm below the pia mater²⁶. After tDCS treatment, the rat was immediately placed under the objective of the two-photon microscope. The fluorescently-labeled solute solution was then introduced into the cerebral circulation by a syringe pump via the carotid artery at a constant flow rate of ~3 mL/min for 1 min in an interval of 5 min (Fig. 1C). 3 mL/min is the normal blood perfusion rate at the rat carotid artery. Simultaneously, the images of the ROI (region of interest) containing the microvessels and surrounding brain tissue were captured when the dye was perfused into the brain. The images of ~239 μm \times 239 μm (512 \times 512) were collected at a rate of ~1 second per image. The corresponding resolution is 0.467 μm \times 0.467 μm /pixel. The collected images were then transferred to an image analysis workstation to determine the BBB solute permeability.

Transcranial Direct Current Stimulation (tDCS) Treatment

tDCS was administered using a constant current stimulator (1 \times 1 tDCS, Soterix Medical Inc, New York, USA) to deliver 3 different doses of weak direct current (0.1, 0.5, and 1 mA) for 20 min (including 30 s ramp up and 30 s ramp down). Specifically, an epicranial anode electrode (1 mm diameter, Ag/AgCl) was positioned into a customized tubular plastic cannula (4 mm inner diameter, 6 mm outer diameter, contact area 0.125 cm²) filled with conductive electrolyte gel (Signa, Parker Laboratory, NJ, USA) and secured stereotactically over the right or left frontal cortex of a rat head (approximately 2 mm anterior to Bregma and 2 mm right to Sagittal suture) (Fig. 1A) using a precise micromanipulator (MM-3 Micromanipulator, Narishige Group, Japan). The returning electrode (5 \times 5 cm adhesive conductive fabric electrode, Axelgaard Manufacturing Co. Ltd. CA, USA) was placed onto the ventral thoracic region of the anaesthetized rat (Fig. 1B). Prior to the placement of the returning electrode, hairs over the thoracic region were removed and a thin layer of Signa gel

was applied, which helped to maintain uniform skin-electrode contact. The corresponding current density for each dosage were 0.8, 4.0 and 8.0 mA/cm². We adopted a unilateral epicranial electrode montage validated in the prior rat models¹⁸. The stimulation intensity range was based on prior safety parameter studies of tDCS in rats¹⁴ and humans¹⁹.

L-NMMA Treatment

To test the effect of L-NMMA on the BBB permeability to different sized solutes, rats were pretreated with 1 mL of 21 mM L-NMMA solution through tail vein injection ~55 min prior to image collection. For a rat of 250–300 g, there is ~20 mL blood. If we inject 1 mL (21 mM) L-NMMA, there is ~1 mM L-NMMA in the blood initially after well mixed. Additionally, in the dye solution injected into the carotid artery, there was 0.1 mM L-NMMA to maintain its effect.

L-NMMA and tDCS treatment

To test whether pretreatment of L-NMMA can abolish the effect of tDCS on the BBB permeability to different sized solutes, rats were pretreated with 1 mL of 21 mM L-NMMA solution through tail vein injection for ~30 min prior to 20 min 1 mA tDCS treatment.

Experimental protocol

Figure 1D summarizes the experimental protocols for three different treatments (tDCS, pretreatment of L-NMMA and tDCS, and L-NMMA only) on the BBB solute permeability. For tDCS treatment, after 20 min 0.1, 0.5 or 1mA tDCS, the rat head was mounted to the multiphoton microscope and the ROI was found in ~ 5 min. The images for determining the BBB solute permeability were first collected ~ 5 min post-tDCS. Then they were continuously collected 1 min in a 5 min interval up to 20 min. For the L-NMMA and tDCS treatment, the rat was pretreated with L-NMMA for ~30 min prior to 20 min 1 mA tDCS. The images were first collected ~ 5 min post tDCS and continuously collected up to 20 min. For L-NMMA treatment only, the images were first collected ~ 55 min post L-NMMA tail injection and continuously collected up to 70 min.

Determination of the BBB solute permeability P

We used the same method as in our previous study²⁶ to determine P of the cerebral microvessels ~100–200 μm below the pia mater. Post-capillary venules of 15–30 μm diameter were chosen for the P measurement³². The reasons that we currently only measured the P of post-capillary venules were: 1) to avoid the influence of smooth muscle cells at arteries, arterioles, and large venules, which would contract under stimuli and affect the P measurement; 2) our previous studies on the BBB permeability were also conducted on this type of post-capillary venules^{26, 32}.

The primary presumption in the calculation of P with the use of fluorescent solutes is that the fluorescence intensity I is a linear function of the number of solute molecules (concentration) in the measuring field. Shi et al^{26,27} found that the relationship between the concentration and the fluorescence intensity was linear from 0.05 to 0.25 mg/mL for sodium fluorescein and from 0.2 to 2 mg/mL for FITC-dextran-70k in the same setting of

multiphoton microscopy used in the current study. We thus used 0.1 mg/mL and 1 mg/mL, respectively, for sodium fluorescein and FITC-dextran-70k in our permeability experiments.

The permeability was determined off-line from the pre-collected images by using ImageJ (National Institutes of Health, Bethesda, MD, USA). Figure 2A shows a typical image of an ROI ($\sim 239 \mu\text{m} \times 239 \mu\text{m}$) with a couple of microvessels and surrounding brain tissue. The total fluorescence intensity in a rectangular window (yellow line enclosed) including a vessel lumen and the surrounding tissue (Fig. 2A) was measured by ImageJ. The measuring window was $\sim 50\text{--}100 \mu\text{m}$ long and $\sim 30\text{--}60 \mu\text{m}$ wide and was set at least $10 \mu\text{m}$ from the base of the bifurcation to avoid solute contamination from the side arms. The criteria for the size and placement of the measuring window were 1) the vessel segment is straight, 2) the dye does not spread out of the window during the time for permeability measurement (5–60 sec), and 3) no dye contamination from the neighboring vessels into the window. When the criteria were satisfied, permeability P was determined using the equation³², $P = I / I_0 * (dI/dt)_0 * r/2$, where I_0 is the step increase of the fluorescence intensity in the window when the dye just fills up the vessel lumen, $(dI/dt)_0$ is the slope of the increasing curve of the total intensity I versus time t when the solute further diffuses into the surrounding tissue, and r is the vessel radius (Fig. 2B). We determined the BBB P to a small solute, sodium fluorescein (MW 376) and a large solute, Dex-70k, which have the representative sizes for the blood-borne molecules and also the similar sizes with the therapeutic agents for treating brain diseases²⁶.

Corrections for influence of red blood cells, free dye, and solvent drag on BBB permeability

The fluorescence dye solution was injected into the brain at a rate of 3 mL/min, the same as the normal blood perfusion rate at the carotid artery³². Although at this perfusion rate the blood was assumed to be replaced by the fluorescence solution, there was still residue blood (red blood cells, RBCs) in the cerebral microvessels, which would overestimate the measured BBB P by $\sim 11\%$, as estimated in³². In addition to RBCs, free dye would overestimate the P to fluorescently labeled solutes³². The influence of the free dye on the solute permeability was estimated by using equation $P_{correct} = [1/(1-F)] P_{measure} - [F/(1-F)] P_{freedye}$, where $P_{measure}$ was measured permeability; $P_{freedye}$ was similar to P^{NaFl} since the molecular weights of FITC (389.4) is close to that of sodium fluorescein (NaFl, 376); $F \sim 0.1\%$ was the intensity ratio of the free dye filtrate to the original fluorescently labeled solution for FITC-dextran 70k; $P_{correct}$ was the corrected solute permeability P .

The above apparent permeability P corrected for the RBCs and free dye still overestimates the true diffusive solute permeability P_d due to the coupling of solute flux with water flow (solvent drag). The P_d for FITC-dex 70k and sodium fluorescein were calculated by using the following equations²⁶,

$$P = P_d \frac{Pe}{\exp(Pe - 1)} + L_p(1 - \sigma)\Delta p_{eff} \quad (1)$$

$$P_e = \frac{L_p(1 - \sigma)\Delta p_{eff}}{P_d} \quad (2)$$

where P is the measured apparent permeability, Pe is the Peclet number, L_p is the hydraulic conductivity of the microvessel, which is $\sim 2.0 \times 10^{-9}$ cm/s/cmH₂O for the cerebral microvessels^{15,26}, σ is the reflection coefficient of the microvessel to the solute, and p_{eff} is the effective filtration pressure across the microvessel wall, obtained from

$$\Delta p_{eff} = \Delta p - \sigma^{albumin} \Delta \pi^{albumin} - \sigma^{dye-solute} \Delta \pi^{dye-solute} \quad (3)$$

where p and π are the hydrostatic and oncotic pressure differences across the microvessel wall. The superscript dye-solute is NaFl or FITC-dextran 70k. σ of rat cerebral microvessels to the test solutes were estimated based on previous studies³² according to the molecule sizes. $\sigma^{dextran-70k}$ (the same as $\sigma^{albumin}$) and σ^{NaFl} were estimated to be 0.95 and 0.1, respectively. p in the cerebral microvessel was ~ 10 cm H₂O, $\pi^{albumin}$ was 3.6 cm H₂O for 10 mg/mL BSA³².

In correcting permeability for the solvent drag, $L_{p,control} = 2 \times 10^{-9}$ cm/s/cmH₂O was used for the control and L-NMMA + tDCS groups. Half of $L_{p,control}$ was used for the L-NMMA only group. Two L_p values, $10 \times L_{p,control}$ and $50 \times L_{p,control}$ were used for the tDCS groups. In fact, the contribution from the solvent drag to the BBB permeability was less than 1% for both solutes under our conditions due to very low L_p .

Data analysis and statistics

P measured under control was averaged as the control P . This value was then used as a reference for all the subsequent treatments. Data were presented as means \pm SE unless otherwise specified. ANOVA was applied to test statistical significance of the treatment over time and to between-group data for permeability differences at specific times. Significance was assumed for probability level $p < 0.05$.

Mathematical model for the paracellular transport across the BBB

The BBB consists of the endothelial cells, the surrounding basement membrane (BM), the wrapping astrocyte foot processes and pericytes. Figure 3 shows its anatomical structure (Fig. 3A) and the simplified model geometry for the paracellular pathway of the BBB (Fig. 3B). Our previous model¹⁷ indicates that the BBB permeability to water and hydrophilic solutes is determined by the structural components in the paracellular pathway of the BBB, i.e., endothelial surface glycocalyx (ESG, thickness L_f) of endothelial cells (ECs), interendothelial cleft (opening width $2B$ and length L), the tight junction between adjacent ECs (opening width $2B_s$ and length L_{jun}), the surrounding BM (thickness $2L_b$ and length $2W_a$), and the gap between astrocyte foot processes (gap width $2B_a$ and length L_a) (Fig. 3B). Due to the very narrow width of the paracellular pathway in the BBB compared to its length, a 1-D model was developed to predict the BBB solute permeability P^1 .

$$P = \frac{1}{R_f + R_{cleft} + R_{jun} + R_{BM} + R_{af}} \times \frac{1}{\pi D_v} \quad (4)$$

Here $R_f = L_f / (2BD_s^f)$, $R_{cleft} = (L - L_{jun}) / (2BD_s^c)$, $R_{jun} = L_{jun} / (2B_s D_s^{jun})$, $R_{BM} = W_a / (4L_b D_s^{BM})$, and $R_{af} = L_a / (2B_a D_s^{af})$ are the resistances of the ESG and each region of the BBB to the solute transport, respectively. D_s^f , D_s^c , D_s^{jun} , D_s^{BM} , and D_s^{af} are the effective solute diffusion coefficients in the ESG, inter-endothelial cleft, small slit in the junction strand, BM, and the cleft between astrocyte foot processes, correspondingly. They can be determined by using the formula in²⁹. D_v is the vessel diameter. The values for the structural dimensions under the control condition can be found in the electron microscopic studies summarized in¹⁷. Briefly, under control, $L_f = 100$ nm, $L = 700$ nm, $L_{jun} = 11$ nm, $L_b = 10$ nm, $L_a = 1000$ nm, $B = 9$ nm, $B_s = 4$ nm, $B_a = 15$ nm and $W_a = 2500$ nm. These parameters were obtained from electron microscopic studies^{1, 12, 25}. For the ESG, its fiber radius is 6 nm and the gap spacing between fibers is 8 nm². We assumed the same structured fiber matrix, or extracellular matrix (ECM) in the BM as in the ESG. Using these values, the model predictions can match the measured BBB permeability to various sized solutes under control¹⁷.

RESULTS

Dose effects of tDCS on BBB permeability

The tDCS current dosage, applied location, and total duration are important factors in controlling the BBB-disruption levels and determining whether the increased BBB permeability is reversible. We set our variables based on prior literature for rats and humans^{14, 19}. Figure 4 shows the temporal effects of tDCS at 0.1, 0.5 and 1 mA, or 0.8, 4.0 and 8.0 mA/cm² on the BBB permeability P to sodium fluorescein (Fig. 4A) and Dex-70k (Fig. 4B), respectively. P was normalized by the control P for each treatment. For the small solute sodium fluorescein, 20 min-0.1 mA tDCS significantly increased the BBB permeability to 4.1 ± 0.3 , 2.9 ± 0.2 , and 1.8 ± 0.3 folds, at 5, 10, and 15 min post tDCS treatment, respectively, P returned to the control in 20 min post tDCS treatment. The increase levels and patterns for P by 20 min-0.5 mA tDCS are similar to those by 0.1 mA tDCS ($p > 0.08$). However, 20 min-1 mA tDCS further increased P to sodium fluorescein to 13.0 ± 1.5 , 9.3 ± 1.6 , and 5.4 ± 0.5 folds, at 5, 10, and 15 min post tDCS treatment, respectively, but P also returned to the control in 20 min post tDCS treatment.

For the large solute Dex-70k, 20 min-0.1 mA tDCS significantly increased the BBB permeability to 9.8 ± 1.8 , 2.6 ± 0.3 , and 2.1 ± 0.3 folds, at 5, 10, and 15 min post tDCS treatment, respectively, P returned to the control in 20 min post tDCS treatment. Different from that for sodium fluorescein, 20 min-0.5 mA tDCS further increased P to Dex-70k to 37.7 ± 9.2 , 16.2 ± 1.9 , and 4.6 ± 0.9 folds, at 5, 10, and 15 min post tDCS treatment, respectively, P returned to the control in 20 min post tDCS treatment. 20 min-1 mA tDCS greatly increased P to Dex-70k to 88.0 ± 10.9 , 57.0 ± 9.3 , and 25.0 ± 2.7 folds, at 5, 10, and 15 min post tDCS treatment, respectively, P also returned to the control in 20 min post tDCS treatment.

Table 1 summarizes the control values for the measured (apparent) P to sodium fluorescein and Dex-70k, and corresponding values after corrected for the RBCs, free dye and solvent drag. Due to very low hydraulic conductivity L_p of the BBB, the contribution from the solvent drag to the P is negligible for both solutes.

Effects of NOS inhibition on BBB permeability

Our previous study showed that ~30 min or longer treatment by 1 mM L-NMMA, an inhibitor of nitric oxide synthase (NOS), can reduce rat mesenteric microvessel permeability to albumin³⁴. To investigate whether L-NMMA has the same effect on the BBB permeability as that on the peripheral microvessel permeability, we injected 1 ml of 21 mM L-NMMA through the rat tail vein, which generated about 1 mM initial blood L-NMMA. After ~55 min from the injection, we determined the BBB permeability to sodium fluorescein and Dex-70k. Figure 5A shows that P to sodium fluorescein reduced to 0.67 ± 0.07 , 0.59 ± 0.06 , 0.60 ± 0.07 , and 0.62 ± 0.08 of the control value, at 55, 60, 65 and 70 min ($p < 0.04$) after L-NMMA injection, respectively. There was no significant difference at different times ($p > 0.4$). Figure 5B shows that P to Dex-70k reduced to 0.66 ± 0.05 , 0.64 ± 0.04 , 0.59 ± 0.06 , and 0.63 ± 0.06 of the control value, at 55, 60, 65 and 70 min ($p < 0.001$) after L-NMMA injection, respectively. There was also no significant difference at different times in P to Dex-70k either ($p > 0.5$).

Combined effects of NOS inhibition and tDCS on BBB permeability

Prior studies have demonstrated that activation of NOS by cytokines or inflammatory agents enhances NO release that increases microvessel permeability^{10, 26}. To test the hypothesis that the increased BBB permeability by tDCS is also due to the release of NO from either the endothelial cells lining the inner wall of the BBB or the nerve cells and glial cells surrounding the endothelial cells, or from both, we pretreated the cerebral microvessels by an inhibitor of NOS, L-NMMA, through tail vein injection for ~30 min before 20 min 1 mA tDCS. Figure 5A demonstrates that pretreatment of L-NMMA did reduce the increase in the BBB permeability P to sodium fluorescein by tDCS. It reduced P from 13.0 ± 1.5 to 3.8 ± 0.3 folds, from 9.3 ± 1.6 to 2.8 ± 0.3 folds, from 5.4 ± 0.5 to 1.9 ± 0.2 folds, respectively, at 5, 10, 15 min post 20 min-1mA tDCS treatment. At 20 min post 20 min-1 mA tDCS, pretreatment of L-NMMA reduced P to 0.64 ± 0.05 of the control ($p = 0.019$). Figure 5B demonstrates that pretreatment of L-NMMA also reduced the increase in the BBB permeability P to Dex-70k by tDCS. It reduced P from 88.0 ± 10.9 to 8.3 ± 0.5 folds, from 57.0 ± 9.3 to 6.4 ± 0.4 folds, from 25.0 ± 2.7 to 4.5 ± 0.2 folds, respectively, at 5, 10, 15 min post 20 min-1mA tDCS treatment. At 20 min post 20 min-1 mA tDCS, pretreatment of L-NMMA reduced P to 0.78 ± 0.07 of the control ($p = 0.03$).

Model predictions for the structural mechanism by which tDCS increases BBB permeability

Figure 6 demonstrates the model predictions for how the BBB structural components contribute to the BBB permeability. If tDCS increases the BBB permeability by degrading the ESG only, Fig. 6A shows negligible increases in P to both solutes. P to NaFl increases by 6% and P to Dex-70k by 4% even after completely removing the ESG ($L_f/L_{f\text{ control}} = 0$). If tDCS additionally degrades the fiber matrix in the BM, it can increase P to NaFl by 2.5-fold

but greatly increase P to Dex-70k by 22.2-fold when the width of the BM is unchanged (Fig. 6B). Increase in the width of the BM further increases P to both solutes. P to NaFl increases by 4.3-fold and P to Dex-70k by 38.6-fold when the width is enlarged by 10-fold and the fiber matrix is completely removed from the BM ($L_f/L_{f\text{ control}} = 0$, $L_b/L_{b\text{ control}} = 10$, no fiber matrix in the BM). If tDCS only additionally enlarges the width of the BM without degrading the fiber matrix in the BM, Fig. 6B shows that it can significantly increase P to both solutes. P to NaFl increases by 3.7-fold and P to Dex-70k by 17.9-fold when the width is enlarged by 10-fold ($L_f/L_{f\text{ control}} = 0$, $L_b/L_{b\text{ control}} = 10$, fiber matrix in the BM). Figure 6C shows the effects of tight junction opening width $2B_s$ on P when the ESG and the fiber matrix in the BM are degraded. When the width of the BM ($2L_b$) is unchanged ($L_b = 10$ nm), increasing $2B_s$ to $2B$ or disrupting tight junctions would increase P to NaFl by 2.5-fold and P to Dex-70k by 24-fold; but would increase P to NaFl by 3.9-fold and P to Dex-70k by 41-fold if the width of the BM ($2L_b$) is enlarged by 4-fold ($L_b = 40$ nm).

It seems that the above modulations in the structural components of the BBB may explain the increase in P to both solutes by 0.1 mA and 0.5 mA tDCS (see Fig. A1 for the comparison between the model predictions and the measured data), but cannot explain the increase in P by 1 mA tDCS. Figure 6D further demonstrates the effects of the interendothelial cleft width $2B$ on the BBB permeability P when the ESG and the fiber matrix in the BM are degraded and the tight junction is disrupted ($2B_s = 2B$). Increasing $2B$ by 10-fold increases P to NaFl by 3.4-fold and P to Dex-70K by 35-fold when the width of the BM ($2L_b$) is unchanged ($L_b = 10$ nm); it increases P to NaFl by 6.6-fold and P to Dex-70k by 91-fold when the width of the BM ($2L_b$) is also increased by 4-fold ($L_b = 40$ nm), and increases P to NaFl by 8-fold and P to Dex-70k by 107-fold when the width of the BM ($2L_b$) is increased by 10-fold ($L_b = 100$ nm). It seems like that the predictions in Fig. 6D can explain the measured BBB permeability under the treatment of 1 mA tDCS.

Comparison of the model predictions with the measured BBB permeability data

Figure 7A compares the model predictions shown in Fig. 6D with the measured BBB permeability P at 5, 10, 15 min post 20-min 1 mA tDCS treatment. We can see from Fig. 7A that 20-min tDCS most likely degrades the ESG and fiber matrix (ECM) in the BM, disrupts the tight junctions, and increases the gap between adjacent endothelial cells ($2B$) and the gap (the width of the BM, $2L_b$) between endothelial cells and the wrapping astrocyte foot processes (see Fig. 5). At 5 min post tDCS, the measured P to Dex-70k is 88.0 ± 10.9 -fold (brown filled triangle) and that to NaFl is 13.0 ± 1.5 -fold (blue filled triangle) of their control values, which are consistent with the predicted P when the $2B$ is 5-fold and $2L_b$ is 4-fold of the controls. At 10 min post tDCS, the measured P to Dex-70K reduces to 57.0 ± 9.3 -fold (brown filled circle) and that to NaFl reduces to 9.3 ± 1.6 -fold (blue filled circle) of their control values, which are consistent with the predicted P when the $2B$ is 1.5-fold and $2L_b$ is 4-fold of the controls. At 15 min post tDCS, the measured P to Dex-70K reduces to 25.0 ± 2.7 -fold (brown filled square) and that to NaFl reduces to 5.4 ± 0.5 -fold (blue filled square) of their control values, which are consistent with the predicted P when the $2B$ and $2L_b$ go back to their control values. Finally, at 20 min post tDCS, the measured P to both solutes return to their control values, which are consistent with the predicted P when the ESG, the ECM in the BM, and the tight junctions restore to their controls (not shown).

Figure 7B compares the measured P with the predicted P for the effects of the NOS inhibition by L-NMMA. Treatments with L-NMMA for ~55 min reduce P to Dex-70k to 0.66 ± 0.05 -fold (blue filled circle), and P to NaFl to 0.67 ± 0.07 -fold (red filled square) of their control values, which are consistent with the predicted P when the resistance of the tight junction increases to 100-fold of the control. L-NMMA is known to enhance the junction integrity³⁴. Figure 7C compares the measured and predicted P , at 5, 10, 15 min post-20 min 1mA tDCS with the ~30 min pretreatment of L-NMMA. At 5, 10 and 15 min post tDCS, pretreatment of L-NMMA (reinforcing the junctions) reduces the increase in P to Dex-70k from 88.0 ± 10.9 -fold to 8.3 ± 0.5 -fold (brown filled triangle), from 57.0 ± 9.3 -fold to 6.4 ± 0.4 -fold (brown filled circle), from 25.0 ± 2.7 -fold to 4.5 ± 0.2 -fold (brown filled square) of their control values, which are consistent with the predicted P when the junction resistance is increased to 30-fold due to 30 min pretreatment of L-NMMA. Correspondingly, at 5, 10 and 15 min post tDCS, pretreatment of L-NMMA reduces the increase in P to NaFl from 13.0 ± 1.5 -fold to 3.8 ± 0.3 -fold (blue filled triangle), from 9.3 ± 1.6 -fold to 2.8 ± 0.3 -fold (blue filled circle), from 5.4 ± 0.5 -fold to 1.9 ± 0.2 -fold (blue filled square) of their control values, which are consistent with the predicted P when the junction resistance is increased due to the pretreatment of L-NMMA.

DISCUSSION

Although effects of tDCS on neuronal activities and brain functions have been widely investigated, the post treatment effect of tDCS on the BBB permeability has never been directly addressed in vivo. In the current study, we employed multiphoton microscopy with a high temporal (one sec per image of area $\sim 239 \mu\text{m} \times 239 \mu\text{m}$) and spatial (sub-micron) resolution to non-invasively and accurately determine the permeability of individual cerebral microvessels in the rat brain, post 20 min treatment of 0.1–1 mA tDCS. We found that tDCS in this dose range and duration significantly and transiently increased the BBB solute permeability. Our results suggest that another mechanism of action (MoA) of tDCS is direct vascular activation, in addition to neuronal polarization as previously found.

tDCS is safe and well tolerated in humans when the established protocols like proper electrode preparation and monitoring of electrode resistance are followed. The dose and duration of the tDCS used in our study were chosen based on the prior studies on rodents¹⁴ and humans¹⁹. Safety limits of tDCS studied on rats showed that a current density of 14.29 mA/cm^2 for duration greater than 10 min produced no pathological brain lesions¹⁸. In our work, we adopted a cathodal tDCS setup on rats similar to that in¹⁸ and delivered 0.1–1 mA (or $0.8\text{--}8 \text{ mA/cm}^2$) tDCS, which is much lower than the safety limit found. tDCS was administered to the right frontal cortex of rat (approximately 2 mm posterior to bregma and 2 mm right to sagittal suture) to obtain similar physiological outcome as that in the human tDCS application studies. Twenty min 1 mA tDCS was widely used in humans and no structural and functional tissue damages were observed²⁴. Hence, contribution of any tDCS related tissue damage to the increased BBB permeability is unlikely. We also measured the temperature increase at the site of tDCS application and that at the site of observation. The temperature increase was less than 2% (from 33°C to less than 33.5°C) at both sites after 20 min 1 mA tDCS treatment. The effect of heat generated by the tDCS is negligible.

To sustain neuronal function, the brain has evolved neurovascular coupling mechanisms to increase the flow of blood to regions in which neurons are activated³. By changing neuronal excitability, tDCS modulates regional cerebral blood flow in humans³¹ and animals²², and enhances blood NO levels¹⁹. DCS on ECs upregulates angiogenic factors such as VEGFs in human umbilical vein ECs⁴ and enhances NO production in bovine aortic ECs³⁰. Our previous study reported that 1 nM VEGF transiently increases the BBB permeability in rats²⁶. Activation of endothelial nitric oxide synthase (eNOS) by cytokines or inflammatory agents and flow-induced shear stresses enhances NO release that increases peripheral microvessel permeability^{10, 34}. tDCS was reported to induce astrocytic Ca²⁺ surges in a transgenic mouse expressing G-CaMP7 in astrocytes²³. The Ca²⁺ can enter into neurons and activate neuronal nitric oxide synthase (nNOS) to release NO and dilate cerebral microvessels⁸. The released NO from neurons may also increase the permeability of cerebral microvessels.

To investigate whether tDCS triggered NO, either from neurons through nNOS or from ECs through eNOS, is responsible for the increase in the BBB permeability by tDCS, we used L-NMMA, an inhibitor for both eNOS and nNOS¹³ to pretreat the cerebral microvessels for 30 min prior to the tDCS treatment. Pretreatment of L-NMMA indeed greatly reduced the BBB permeability increased by tDCS. This result indicates that the tDCS-enhanced BBB permeability is NO dependent.

Mayhan²¹ found that the basal permeability of the rat pial microvessel to various sized solutes was not altered by topical application of 10 and 100 μ M L-NMMA for 20–60 min. Our current study found that the basal permeability of the BBB to sodium fluorescein and Dex-70k reduced to ~65% after 55–70 min L-NMMA treatment with ~1 mM initial concentration through the tail injection for ~55 min and 100 μ M in the perfusate through the carotid artery infusion afterwards. The different findings may come from 1) a higher concentration of L-NMMA used in our current study; 2) the different application methods, one is by topical application of L-NMMA on the pial microvessel, which needs craniotomy and another by perfusion to the cerebral microvessels 100–200 μ m below pial mater, which does not need craniotomy. Easton et al¹¹ found that the permeability of the pial microvessel to Lucifer Yellow rose to 8 times in 20–60min following the craniotomy. The topical application of L-NMMA may just compensate the permeability increase by craniotomy in Mayhan²¹; and 3) Our recent study in Zhang et al³⁴ indicated that perfusion of 1 mM L-NMMA into an individually cannulated rat mesenteric microvessel slightly increased the permeability to albumin initially, but reduced the permeability after 35 min perfusion. In the current study, the permeability was measured after ~55 min L-NMMA treatment.

Our results show that the tDCS-induced BBB permeability fold increase to a small solute, sodium fluorescein with molecular weight 376, is much lower than that to a large solute, Dex-70k. To explain these observed data and to investigate the transient structural changes in the BBB by tDCS, we employed a previously developed mathematical model for the paracellular transport across the BBB to predict the possible changes. Comparison of the model prediction with the measured data suggests that tDCS increase the BBB permeability by transiently degrading the endothelial surface glycocalyx (ESG) and the extracellular matrix (ECM) in the BM, disrupting the endothelial junctions, and enlarging the gap

between endothelial cells (ECs) and that between ECs and astrocyte foot processes. These structural changes may be due to the contraction of ECs induced by tDCS through astrocytic Ca^{2+} surges²³ and NO release^{19, 30}. The tDCS-induced BBB permeability increase is reversible. It returns to the control for both small and large solutes 20 min post treatment. Figure 7A shows that the reversal starts from recovering the increased gap between ECs and that between ECs and astrocyte foot processes, then EC junctions are reconstructed, finally the ESG and ECM in the BM are restored. ESG lining the inner wall of all the blood vessels is a dynamic structure which can be degraded, reinforced and restored by the blood-borne components³³. It is almost impossible to examine in vivo if the ESG and ECM are degraded by the tDCS, however, we may test it by using our in vitro BBB model¹⁶ in the future study.

The decreased microvessel permeability by NOS inhibitor L-NMMA is likely due to the formation of more EC junctions³⁴. Thus we used the model shown in Fig. 3 by increasing the resistance of the EC junctions to predict the effects of L-NMMA treatment alone and pretreatment along with tDCS on the BBB permeability. Reinforcing the EC junctions by L-NMMA not only decreases the BBB basal permeability, but also greatly reduces the tDCS-induced increase in the BBB permeability (Figs. 7B, C).

In conclusion, our results conform to our hypothesis that tDCS transiently increases the BBB permeability, suggesting another mechanism of action of tDCS by direct vascular activation. The permeability increase by the tDCS is NO dependent and reversible. Our findings also suggest that tDCS at proper dose and duration can be used as a convenient, non-invasive, and selective approach for systemic drug delivery to the central nervous system via the BBB.

Acknowledgements

We thank the technique assistance from Dr. Lingyan Shi and Ms. Min Zeng. This work was supported by the U.S. National Institutes of Health grants R21EB017510 (BMF and MB), 1SC1CA153325 (BMF) and R01 NS101362 (BMF and MB).

Appendix

We used the following empirical formula, which were generated by rigorous theoretical models from hydrodynamics and transport phenomena and summarized in (Sugihara-Seki and Fu, 2005)²⁹, to estimate the effective solute diffusion coefficients in different regions of the BBB (Fig. 3B). The basic concept is that the diffusion transport of a solute is retarded by the friction between the solute and the walls/fibers and by the steric hindrance due to the existence of the walls and the fibers. The effective solute diffusion coefficient thus changes with the sizes of cleft/slit, fiber matrix porosity/arrangements and the solute sizes.

In the endothelial surface glycocalyx region,

$$\frac{D_{fiber}}{D_{free}} = 1 - \left[(1 - \varepsilon)^{0.5} \left(1 + \frac{2a}{\pi^{0.5} r_f} \right) \right] \quad (A1)$$

Here, a is the solute radius, r_f is the fiber radius, S_f is the volume fraction of fibers, $\varepsilon = 1 - S_f$ is the void volume fraction. D_{free} is the solute diffusion coefficient in free aqueous solution at 37°C in our study (Li et al, 2010)¹⁷.

In the inter-endothelial cleft, junction slit and the cleft between astrocyte foot processes, as well as in the basement membrane (BM) without ECM,

$$\frac{D_{cleft}}{D_{free}} = (1 - \beta) * (1 - 1.004\beta + 0.418\beta^3 + 0.210\beta^4 - 0.1696\beta^5) \quad (A2)$$

Here, $\beta = 2a/W$, a is the solute radius and W is the cleft/slit width or the BM width.

In the BM with ECM,

$$\frac{D_{BM}}{D_{free}} = \left\{ 1 - \left[(1 - \varepsilon)^{0.5} \left(1 + \frac{2a}{\pi^{0.5} r_f} \right) \right] \right\} * (1 - \beta) * (1 - 1.004\beta + 0.418\beta^3 + 0.210\beta^4 - 0.1696\beta^5) \quad (A3)$$

Table A1 summarizes the anatomical parameters of the BBB under control, which were used to calculate the effective solute diffusion coefficients (Table A2) and resistances (Table A3) in five regions of the BBB (Eq.4 in the main text), by employing the corresponding Eqs. A1–A3.

Table A1

Anatomical parameters of the BBB under control (from Li et al, 2010, see Fig. 3B)

| | | |
|---|-----------|-----------|
| Vessel diameter | D_v | 10,000 nm |
| Endothelial surface glycocalyx (ESG) thickness | L_f | 100 nm |
| Glycocalyx fiber radius | r_f | 6 nm |
| Fiber volume fraction of ESG | S_f | 0.326 |
| Total length of the cleft region | L | 700 nm |
| Distance between the tight junction strand and the front of the inter-endothelial cleft | L_1 | 350 nm |
| Thickness of the tight junction strand | L_{jun} | 11 nm |
| Width of the inter-endothelial cleft | $2B$ | 18 nm |
| Width of the small slit of the tight junction | $2B_s$ | 8 nm |
| Thickness of the basement membrane | $2L_b$ | 20 nm |
| Thickness of astrocyte foot processes | L_a | 1000 nm |
| Width of the cleft between astrocyte foot processes | $2B_a$ | 30 nm |
| Length of astrocyte foot processes | $2W_a$ | 5000 nm |

Table A2

Effective diffusion coefficients for each region of the BBB under control

| | NaFl | Dex-70k |
|---|---|---|
| Solute radius | 0.45 nm | 3.5 nm |
| D_{free} at 37°C | $56.2 \times 10^{-7} \text{ cm}^2/\text{s}$ | $7.23 \times 10^{-7} \text{ cm}^2/\text{s}$ |
| Ratio of $D_{\text{eff}}/D_{\text{free}}$ in 5 regions of the BBB | | |
| D_s^f (ESG)/ D_{free} | 0.24 | 0.053 |
| D_s^c (inter-endothelial cleft)/ D_{free} | 0.90 | 0.64 |
| D_s^{jun} (tight junction slit)/ D_{free} | 0.79 | 0.44 |
| D_s^{BM} (BM with ECM)/ D_{free} | 0.22 | 0.036 |
| D_s^{af} (cleft between astrocyte foot processes)/ D_{free} | 0.94 | 0.59 |

Table A3

Resistance from each region of the BBB under control

| | NaFl | Dex-70k |
|--|------------------------------------|------------------------------------|
| R_f (ESG) | 23.4 (s/cm ²) | 104.4 (s/cm ²) |
| R_{cleft} (inter-endothelial cleft) | 42.4 (s/cm ²) | 98.3 (s/cm ²) |
| R_{jun} (tight junction slit) | 1.75 (s/cm ²) | 25.1 (s/cm ²) |
| R_{BM} (BM with ECM) | 577.7(s/cm ²) | 1756.1(s/cm ²) |
| R_{af} (cleft between astrocyte foot processes) | 35.4 (s/cm ²) | 56.4 (s/cm ²) |
| Predicted BBB permeability under control | $26.3 \times 10^{-7} \text{ cm/s}$ | $1.13 \times 10^{-7} \text{ cm/s}$ |

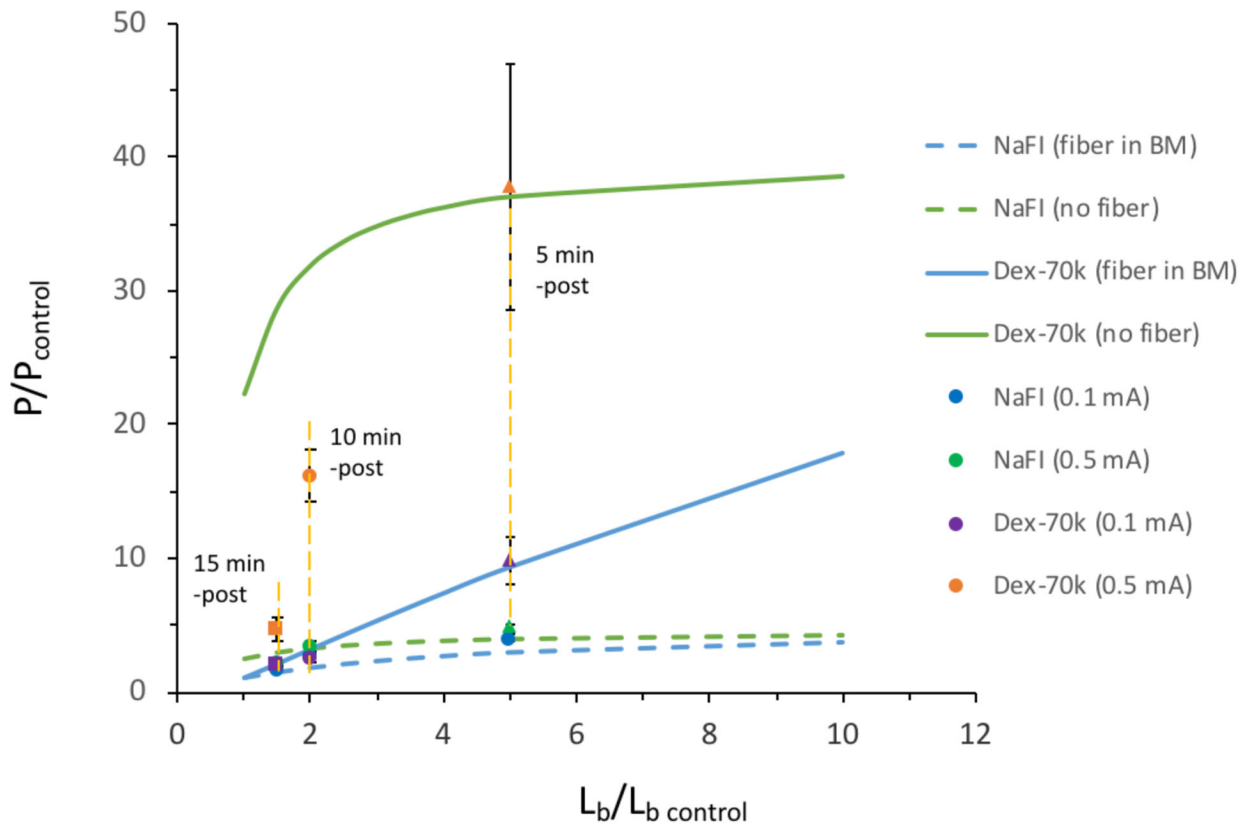


Fig. A1.

Comparison of the model predictions (lines) with the experimental results (symbols) for the effects of 0.1 mA and 0.5 mA tDCS on the BBB permeability P . The lines are the model predictions for the cases of increasing basement membrane (BM) thickness L_b in addition to degrading the ESG. The solid lines are for Dex-70k and the dashed lines for NaFl. The blue lines are for the cases when the fiber matrix is intact in the BM and the green lines are for the cases when the fiber matrix is disrupted in the BM. The blue and green colored symbols are the measured permeability data for NaFl, 5, 10, 15 min post-0.1 mA and post-0.5 mA tDCS, respectively, while the purple and orange colored symbols are the measured permeability data for Dex-70k, 5, 10, 15 min post-0.1 mA and post-0.5 mA tDCS, respectively.

REFERENCE

1. Adamson RH, Lenz JF, Zhang X, Adamson GN, Weinbaum S, and Curry FE. Oncotic pressures opposing filtration across non-fenestrated rat microvessels. *J Physiol.* 557:889–907, 2004. [PubMed: 15073281]
2. Arkill KP, Knupp C, Michel CC, Neal CR, Qvortrup K, Rostgaard J, and Squire JM. Similar endothelial glycocalyx structures in microvessels from a range of mammalian tissues: evidence for a common filtering mechanism? *Biophys J.* 101:1046–56, 2011. [PubMed: 21889441]
3. Attwell D, Buchan AM, Charpak S, Lauritzen M, Macvicar BA, and Newman EA. Glial and neuronal control of brain blood flow. *Nature.* 468:232–43, 2010. [PubMed: 21068832]
4. Bai H, Forrester JV, and Zhao M. DC electric stimulation upregulates angiogenic factors in endothelial cells through activation of VEGF receptors. *Cytokine.* 55:110–5, 2011. [PubMed: 21524919]

5. Bikson M, Grossman P, Thomas C, Zannou AL, Jiang J, Adnan T, Mourdoukoutas AP, Kronberg G, Truong D, Boggio P, Brunoni AR, Charvet L, Fregni F, Fritsch B, Gillick B, Hamilton RH, Hampstead BM, Jankord R, Kirton A, Knotkova H, Liebetanz D, Liu A, Loo C, Nitsche MA, Reis J, Richardson JD, Rotenberg A, Turkeltaub PE, and Woods AJ. Safety of Transcranial Direct Current Stimulation: Evidence Based Update 2016. *Brain Stimul.* 9:641–661, 2016. [PubMed: 27372845]
6. Boggio PS, Berman F, Vergara AO, Muniz AL, Nahas FH, Leme PB, Rigonatti SP, and Fregni F. Go-no-go task performance improvement after anodal transcranial DC stimulation of the left dorsolateral prefrontal cortex in major depression. *J Affect Disord.* 101:91–8, 2007. [PubMed: 17166593]
7. Brunoni AR, Nitsche MA, Bolognini N, Bikson M, Wagner T, Merabet L, Edwards DJ, Valero-Cabre A, Rotenberg A, Pascual-Leone A, Ferrucci R, Priori A, Boggio PS, and Fregni F. Clinical research with transcranial direct current stimulation (tDCS): challenges and future directions. *Brain Stimul.* 5:175–195, 2012. [PubMed: 22037126]
8. Busija DW, Bari F, Domoki F, and Louis T. Mechanisms involved in the cerebrovascular dilator effects of N-methyl-d-aspartate in cerebral cortex. *Brain Res Rev.* 56:89–100, 2007. [PubMed: 17716743]
9. Cancel LM, Arias K, Bikson M, and Tarbell JM. Direct current stimulation of endothelial monolayers induces a transient and reversible increase in transport due to the electroosmotic effect. *Scientific reports.* 8:9265, 2018. [PubMed: 29915178]
10. Duran WN, Breslin JW, and Sanchez FA. The NO cascade, eNOS location, and microvascular permeability. *Cardiovasc Res.* 87:254–61, 2010. [PubMed: 20462865]
11. Easton AS, Sarker MH, and Fraser PA. Two components of blood-brain barrier disruption in the rat. *J Physiol.* 503 (Pt 3):613–23, 1997. [PubMed: 9379415]
12. Farkas E and Luiten PG. Cerebral microvascular pathology in aging and Alzheimer's disease. *Prog Neurobiol.* 64:575–611, 2001. [PubMed: 11311463]
13. Forstermann U and Sessa WC. Nitric oxide synthases: regulation and function. *Eur Heart J.* 33:829–37, 837a–837d, 2012. [PubMed: 21890489]
14. Jackson MP, Truong D, Brownlow ML, Wagner JA, McKinley RA, Bikson M, and Jankord R. Safety parameter considerations of anodal transcranial Direct Current Stimulation in rats. *Brain Behav Immun.* 64:152–161, 2017. [PubMed: 28427911]
15. Kimura M, Dietrich HH, Huxley VH, Reichner DR, and Dacey RG Jr. Measurement of hydraulic conductivity in isolated arterioles of rat brain cortex. *Am J Physiol.* 264:H1788–97, 1993. [PubMed: 8322907]
16. Li G, Simon MJ, Cancel LM, Shi ZD, Ji X, Tarbell JM, Morrison B 3rd, and Fu BM. Permeability of endothelial and astrocyte cocultures: in vitro blood-brain barrier models for drug delivery studies. *Ann Biomed Eng.* 38:2499–511, 2010. [PubMed: 20361260]
17. Li G, Yuan W, and Fu BM. A model for the blood-brain barrier permeability to water and small solutes. *J Biomech.* 43:2133–40, 2010. [PubMed: 20434157]
18. Liebetanz D, Koch R, Mayenfels S, Konig F, Paulus W, and Nitsche MA. Safety limits of cathodal transcranial direct current stimulation in rats. *Clin Neurophysiol.* 120:1161–7, 2009. [PubMed: 19403329]
19. Marceglia S, Mrakic-Spota S, Rosa M, Ferrucci R, Mameli F, Vergari M, Arlotti M, Ruggiero F, Scarpini E, Galimberti D, Barbieri S, and Priori A. Transcranial Direct Current Stimulation Modulates Cortical Neuronal Activity in Alzheimer's Disease. *Front Neurosci.* 10:134, 2016. [PubMed: 27065792]
20. Marquez-Ruiz J, Leal-Campanario R, Sanchez-Campusano R, Molaee-Ardekani B, Wendling F, Miranda PC, Ruffini G, Gruart A, and Delgado-Garcia JM. Transcranial direct-current stimulation modulates synaptic mechanisms involved in associative learning in behaving rabbits. *Proc Natl Acad Sci U S A.* 109:6710–5, 2012. [PubMed: 22493252]
21. Mayhan WG Inhibition of nitric oxide synthase does not alter basal permeability of the blood-brain barrier. *Brain Res.* 855:143–9, 2000. [PubMed: 10650141]
22. Mielke D, Wrede A, Schulz-Schaeffer W, Taghizadeh-Waghefi A, Nitsche MA, Rohde V, and Liebetanz D. Cathodal transcranial direct current stimulation induces regional, long-lasting reductions of cortical blood flow in rats. *Neurol Res.* 35:1029–37, 2013. [PubMed: 23899548]

23. Monai H, Ohkura M, Tanaka M, Oe Y, Konno A, Hirai H, Mikoshiba K, Itohara S, Nakai J, Iwai Y, and Hirase H. Calcium imaging reveals glial involvement in transcranial direct current stimulation-induced plasticity in mouse brain. *Nat Commun.* 7:11100, 2016. [PubMed: 27000523]
24. Nitsche MA and Paulus W. Sustained excitability elevations induced by transcranial DC motor cortex stimulation in humans. *Neurology.* 57:1899–901, 2001. [PubMed: 11723286]
25. Schulze C and Firth JA. Interendothelial junctions during blood-brain barrier development in the rat: morphological changes at the level of individual tight junctional contacts. *Brain Res Dev Brain Res.* 69:85–95, 1992. [PubMed: 1424091]
26. Shi L, Zeng M, and Fu BM. Temporal effects of vascular endothelial growth factor and 3,5-cyclic monophosphate on blood-brain barrier solute permeability in vivo. *J Neurosci Res.* 92:1678–89, 2014. [PubMed: 25066133]
27. Shi L, Zeng M, Sun Y, and Fu BM. Quantification of blood-brain barrier solute permeability and brain transport by multiphoton microscopy. *J Biomech Eng.* 136:031005, 2014. [PubMed: 24193698]
28. Stagg CJ, Lin RL, Mezue M, Segerdahl A, Kong Y, Xie J, and Tracey I. Widespread modulation of cerebral perfusion induced during and after transcranial direct current stimulation applied to the left dorsolateral prefrontal cortex. *J Neurosci.* 33:11425–31, 2013. [PubMed: 23843514]
29. Sugihara-Seki M and Fu BMM. Blood flow and permeability in microvessels. *Fluid Dynamics Research.* 37:82–132, 2005.
30. Trivedi DP, Hallock KJ, and Bergethon PR. Electric fields caused by blood flow modulate vascular endothelial electrophysiology and nitric oxide production. *Bioelectromagnetics.* 34:22–30, 2013. [PubMed: 22674251]
31. Wang Y, Hao Y, Zhou J, Fried PJ, Wang X, Zhang J, Fang J, Pascual-Leone A, and Manor B. Direct current stimulation over the human sensorimotor cortex modulates the brain's hemodynamic response to tactile stimulation. *Eur J Neurosci.* 42:1933–40, 2015. [PubMed: 25989209]
32. Yuan W, Lv Y, Zeng M, and Fu BM. Non-invasive measurement of solute permeability in cerebral microvessels of the rat. *Microvasc Res.* 77:166–73, 2009. [PubMed: 18838082]
33. Zeng Y, Zhang XF, Fu BM, and Tarbell JM. The Role of Endothelial Surface Glycocalyx in Mechanosensing and Transduction, in *Molecular, Cellular, and Tissue Engineering of the Vascular System.* 2018, Springer p. 1–27.
34. Zhang L, Zeng M, and Fu BM. Inhibition of endothelial nitric oxide synthase decreases breast cancer cell MDA-MB-231 adhesion to intact microvessels under physiological flows. *Am J Physiol Heart Circ Physiol.* 310:H1735–47, 2016. [PubMed: 27059076]

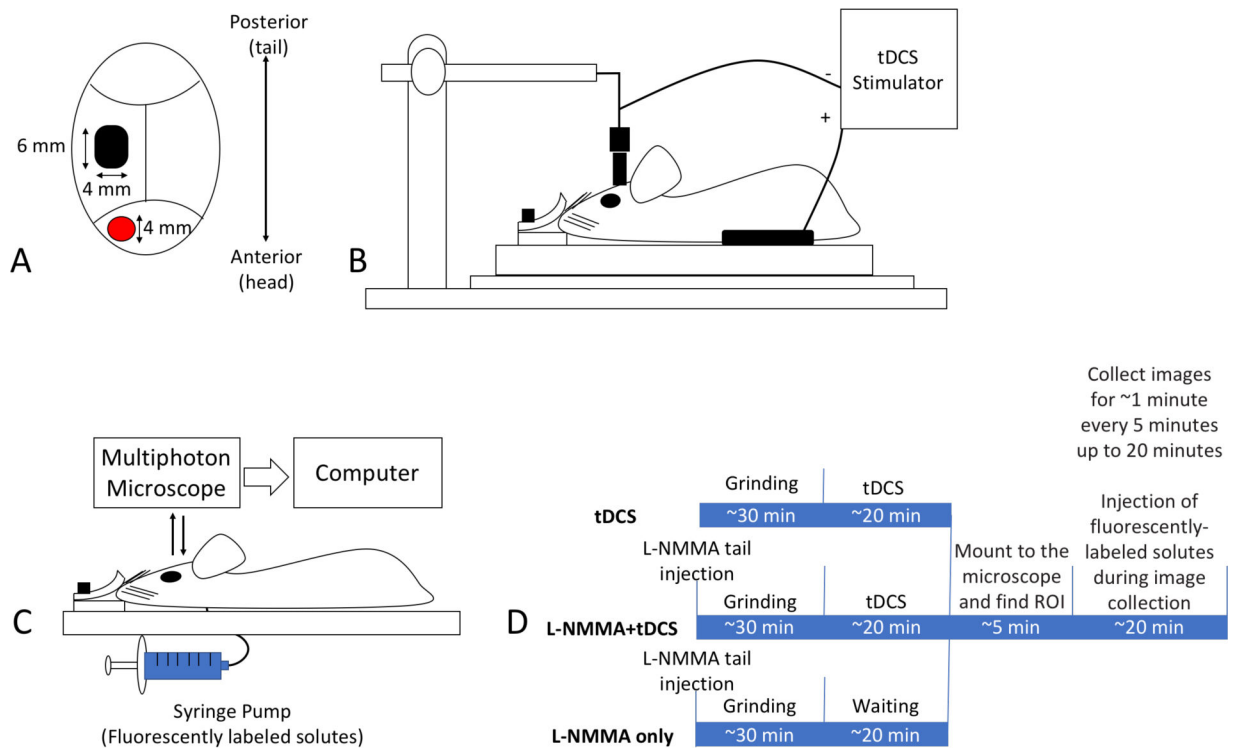


Fig. 1. Illustration of experimental setups and protocols.

(A) Schematic of the rat skull showing the locations for the tDCS treatment and multiphoton imaging. The red circled area is the region of the tDCS application and the black rectangular ellipse represents the region of the thinned skull for the microscope imaging for the BBB permeability measurement. (B) Schematic of the setup for the tDCS application to the rat brain. One electrode connects to the rat cranium (the red circled area) shown in (A) and the counter electrode connects to the ventral thoracic region. (C) Schematic of the BBB solute permeability measurement by multiphoton microscopy. While the solution with the fluorescently labeled solute is injected through the carotid artery at a rate of ~ 3 mL/min, the images of the ROI containing several microvessels and the surrounding brain tissue are collected. The ROI is in the cerebral cortex 100–200 μm below the pia mater in the region indicated by the black rectangular ellipse in (A). The BBB permeability is determined off-line by analyzing the collected images (shown in Fig. 2). (D) Experimental timelines and protocols for the BBB permeability measurement under various treatments.

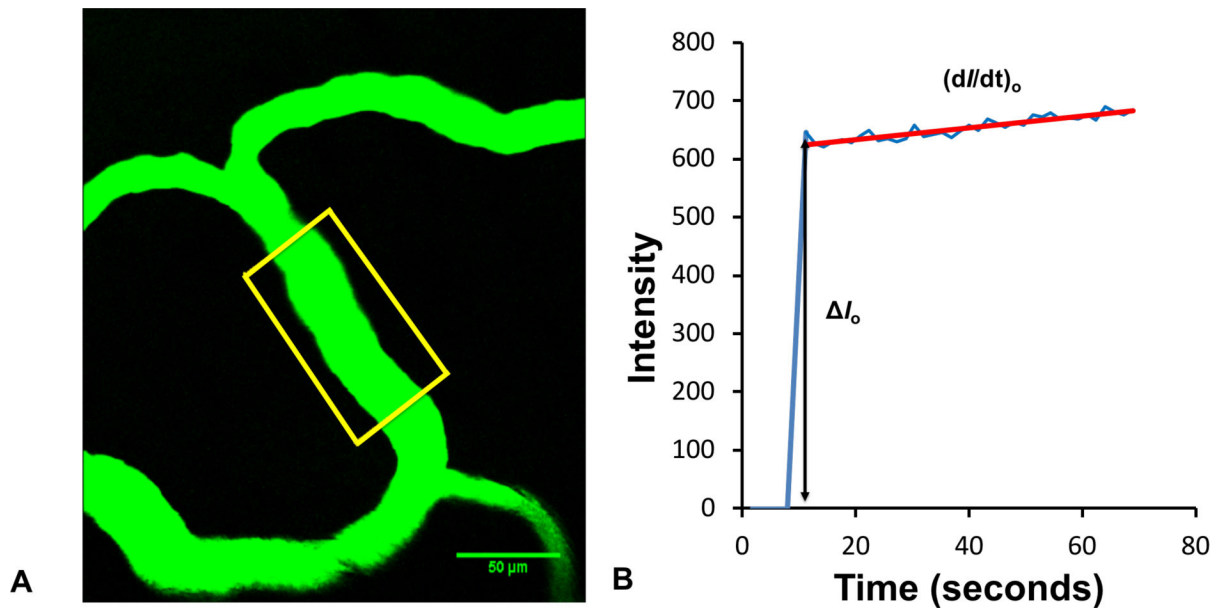


Fig. 2. Determination of the BBB solute permeability P .

(A) Illustration of the scanning region of interest (ROI) comprising several microvessels, $\sim 100\text{--}200\ \mu\text{m}$ below the pia mater. The scanning ROI is $\sim 239\ \mu\text{m} \times 239\ \mu\text{m}$. The orange frame enclosed area is the ROI used to determine the BBB permeability to a solute. (B) Total fluorescence intensity in the yellow frame enclosed ROI as a function of the perfusion time. Fluorescence intensity in the figure is proportional to the total amount of the solutes accumulated in the measuring region surrounding the microvessel. The slope of the regression line over the initial linear accumulation $(dI/dt)_0$ (red line) is used to determine the solute permeability $P = 1/ I_0 * (dI/dt)_0 * r/2$, where I_0 (black line with arrowheads) is the step intensity increase when the dye just fills up the vessel lumen, and r is the radius of the vessel.

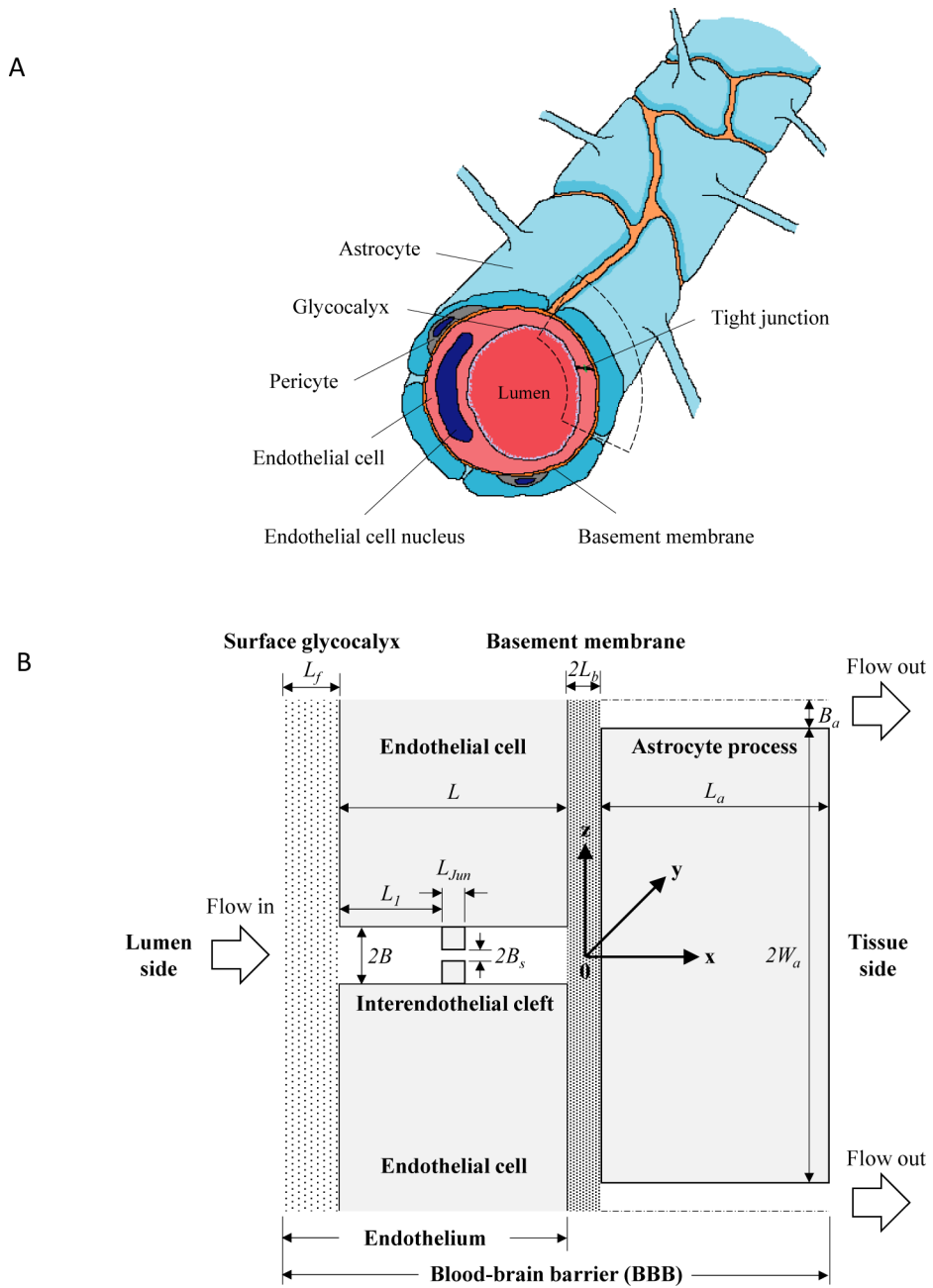


Fig. 3. The BBB structure and the simplified model geometry for the paracellular transport. (A) Three dimensional sketch of a cerebral microvessel. Its wall (the BBB) is formed by endothelial cells, basement membrane, pericytes and astrocyte foot processes. Based on the electron microscopic observation in Farkas and Luiten (2001). (B) Simplified model geometry for the paracellular pathway of the BBB (dashed line enclosed area in A). The interendothelial cleft has a length of L and a width of $2B$. The tight junction strand inside the cleft has a length of L_{Jun} and a width of $2B_s$. The distance between the junction strand and luminal front of the cleft is L_1 . The thickness of the endothelial surface glycocalyx is L_f . The width of the basement membrane is $2L_b$ and the length of the astrocyte foot processes is

$2W_a$. The gap between astrocyte foot processes has a length of L_a and a width of $2B_a$.
Revised from Li et al (2010b).

Author Manuscript

Author Manuscript

Author Manuscript

Author Manuscript

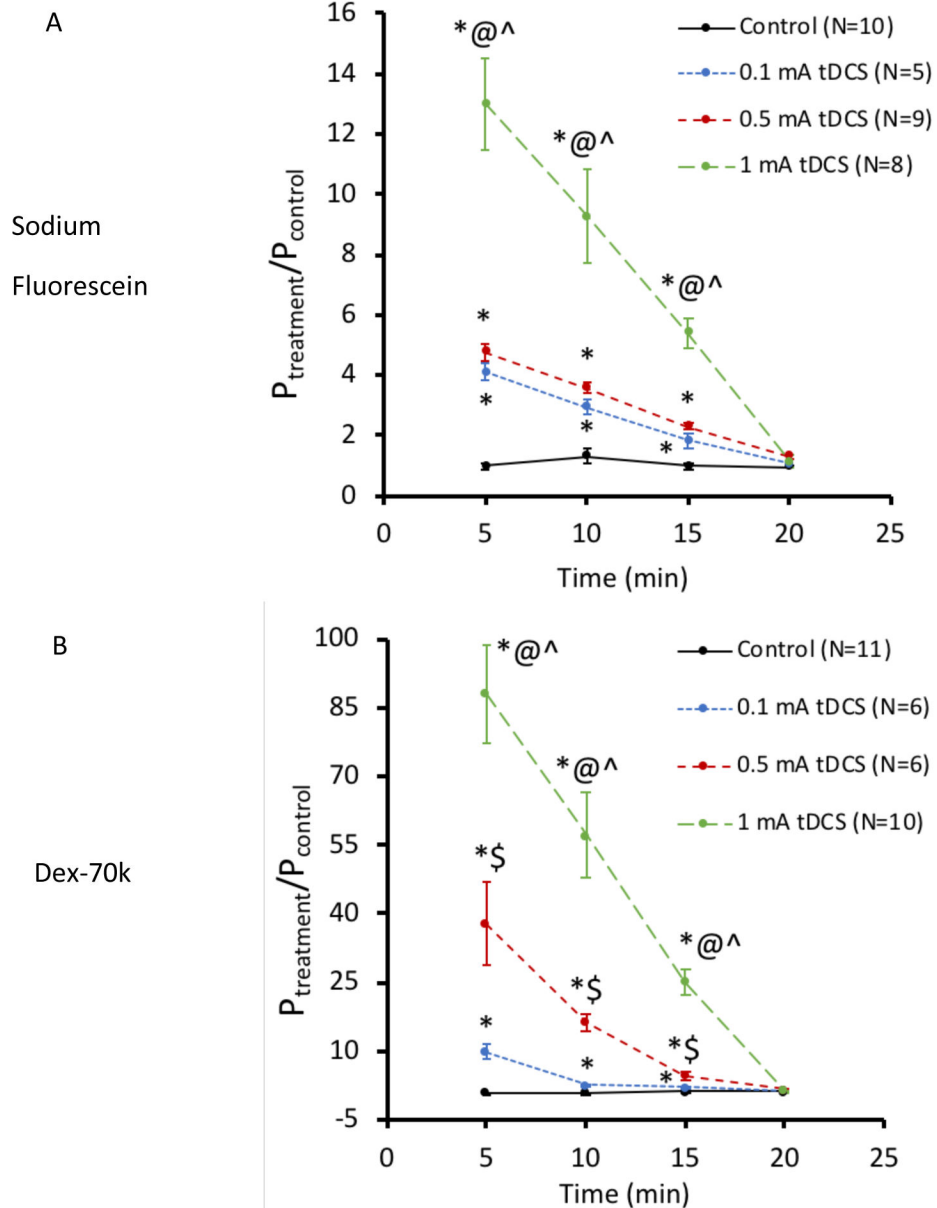


Fig. 4. Effects of tDCS strength on the BBB permeability.

Normalized BBB permeability as a function of time for the control and tDCS treatment with various doses for (A) sodium fluorescein and (B) FITC-dextran 70k. * $p < 0.05$ compared with the control; @ $p < 0.05$ comparing 0.1 mA with 1 mA; ^ $p < 0.05$ comparing 0.5 mA with 1 mA; \$ $p < 0.05$ comparing 0.1 mA with 0.5 mA.

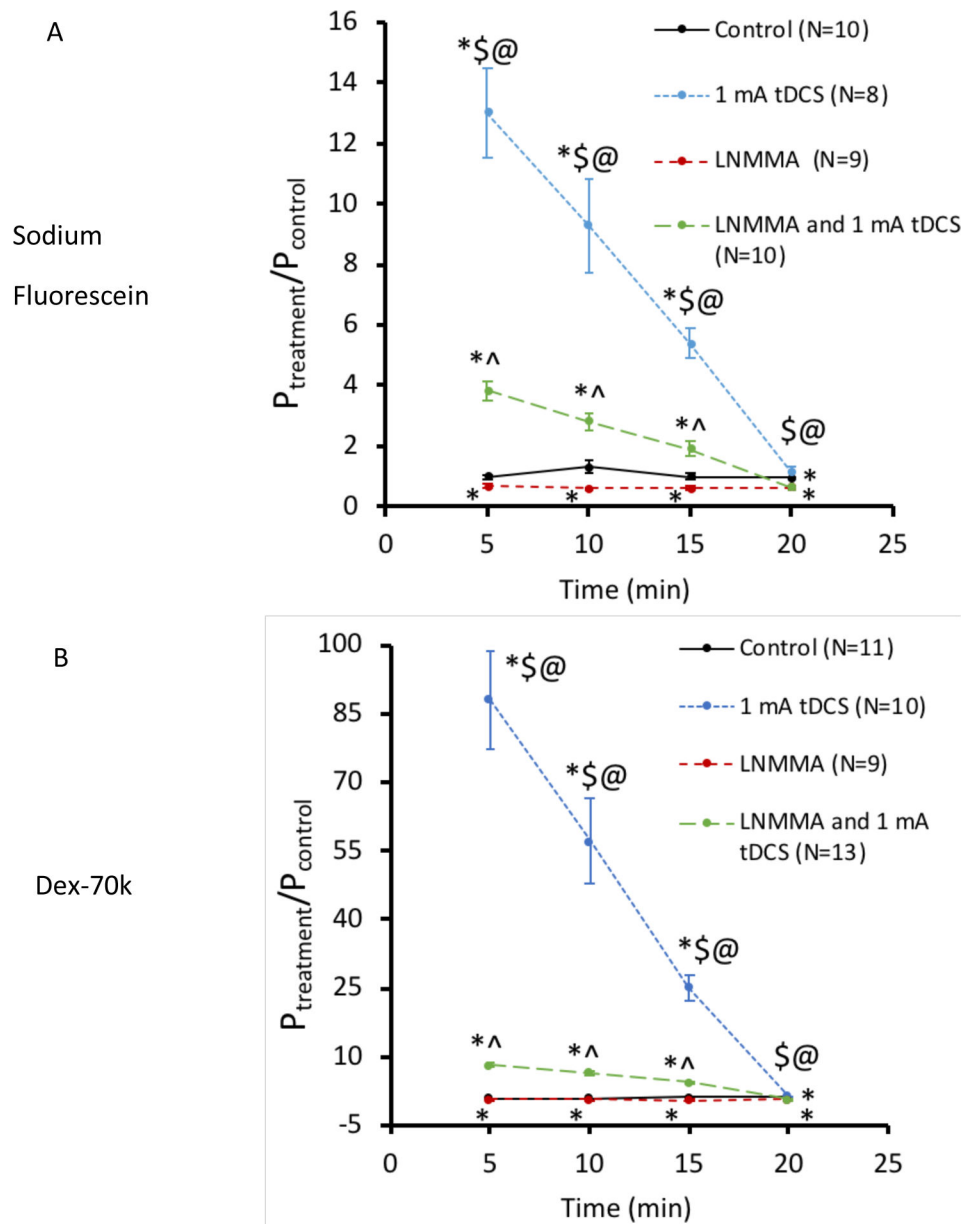


Fig. 5. Effects of NOS inhibitor (L-NMMA) and tDCS with pretreatment of L-NMMA on the BBB permeability.

Normalized BBB permeability as a function of time for the control and treatment groups for (A) sodium fluorescein and (B) FITC-dextran 70k. * $p < 0.05$ compared with the corresponding control; @ $p < 0.05$ comparing 1 mA tDCS with L-NMMA pretreatment and 1 mA tDCS; ^ $p < 0.05$ comparing L-NMMA only with L-NMMA pretreatment and 1 mA tDCS; \$ comparing 1 mA tDCS with L-NMMA only.

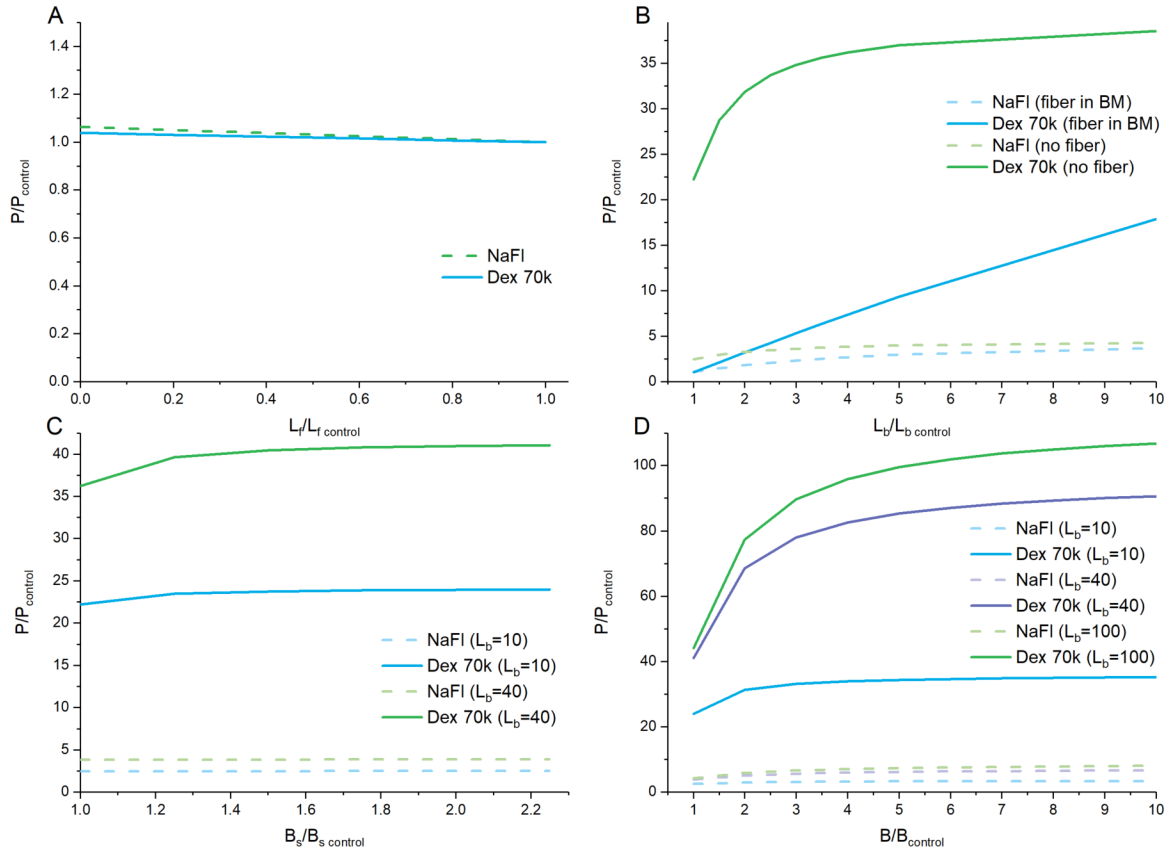


Fig. 6. Model predictions for the BBB permeability P .

For P to sodium fluorescein and FITC-dextran 70k as a function of the endothelial surface glycocalyx thickness L_f (**A**); as a function of the basement membrane thickness $2L_b$ when the surface glycocalyx is degraded and when the fiber matrix in the basement membrane is or is not degraded (**B**); as a function of the tight junction opening width $2B_s$ when the glycocalyx and the fiber matrix in the basement membrane are degraded (**C**); and as a function of the interendothelial cleft width $2B$ when the glycocalyx and the fiber matrix in the basement membrane are degraded and the junction is disrupted ($B_s = B$) (**D**).

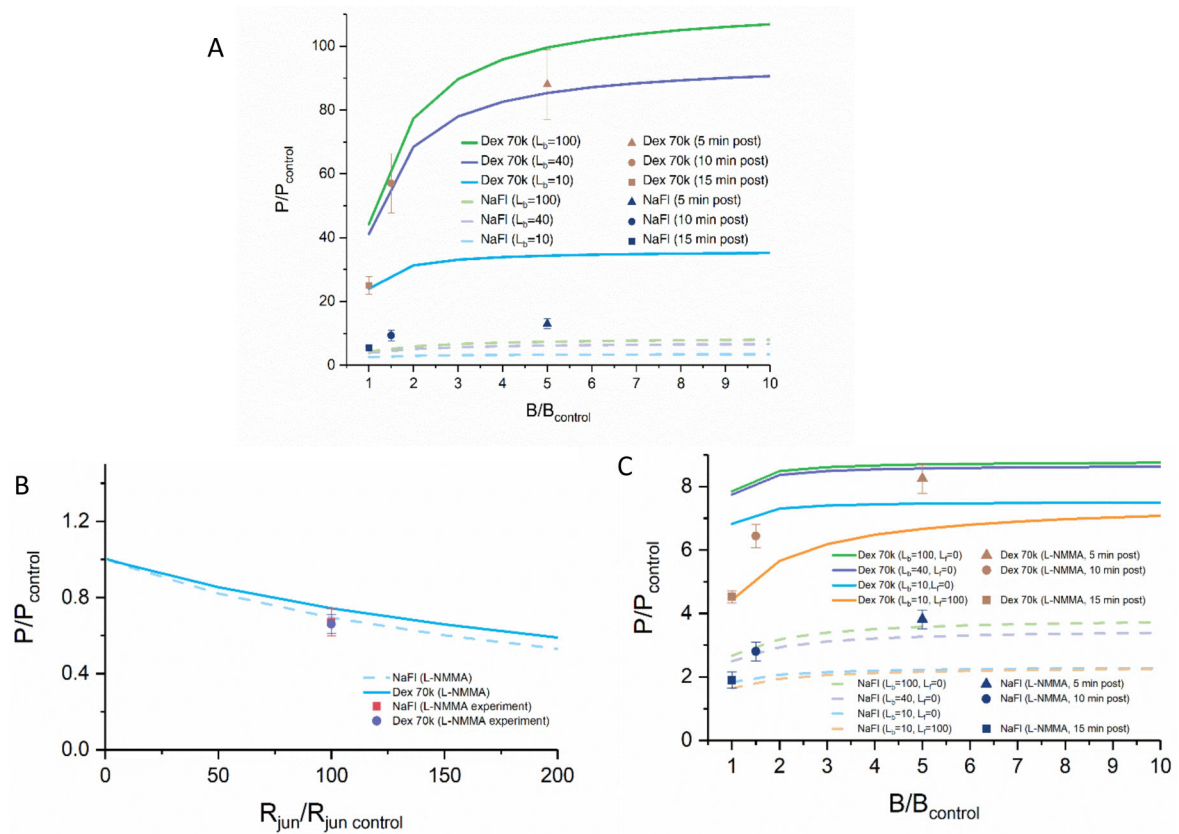


Fig. 7. Comparison of model predictions with experimental results for the effects of tDCS, L-NMMA and tDCS with L-NMMA on the BBB permeability P .

(A) Effects of tDCS. The lines are model predictions for the case of increasing the interendothelial cleft width $2B$ and the basement membrane width $2L_b$ when the glycocalyx and fiber matrix in the basement membrane are degraded, and the junction is disrupted ($B_s = B$). The solid lines are for P to FITC-dextran 70k and the dashed lines for P to sodium fluorescein. The symbols are the measured data 5, 10 and 15 min post 20-min 1 mA tDCS treatment (mean \pm SE). The brown colored symbols for P to FITC-dextran 70k and the blue colored symbols for P to sodium fluorescein. (B) Effects of L-NMMA treatment only and (C) effects of tDCS after L-NMMA pretreatment on the BBB permeability. In (B), the lines are the model predictions (solid line for Dex-70K and dashed line for sodium fluorescein) for the case of increasing junction strand resistance R_{jun} in the interendothelial cleft. The symbols are measured data after ~ 55 min 1 mM L-NMMA treatment (mean \pm SE). In (C), the lines are the model predictions (solid lines for Dex-70K and dashed lines for sodium fluorescein) for the case of increasing junction strand resistance R_{jun} to 30-fold of the control, and increasing the interendothelial cleft width $2B$ and the basement membrane width $2L_b$. The symbols are the measured data 5, 10 and 15 min post 20-min 1 mA tDCS treatment after ~ 30 min 1 mM L-NMMA pretreatment (mean \pm SE).

Table 1Measured and corrected control P

| Solute | N | Vessel Radius (μm) | P (measured) ($\times 10^{-7}$ cm/s) | P (Corrected for RBC) ($\times 10^{-7}$ cm/s) | P (Corrected for RBC and Free Dye) ($\times 10^{-7}$ cm/s) | P_d (Corrected for RBC, Free Dye, and Solvent Drag) ($\times 10^{-7}$ cm/s) |
|--------------------|----|---------------------------------|---------------------------------------|--|---|--|
| Sodium Fluorescein | 10 | 9.5 \pm 1.3 | 18.70 \pm 2.36 | 16.85 \pm 2.13 | 16.85 \pm 2.13 | 16.85 \pm 2.13 ($L_{p,\text{control}}=2\times 10^{-9}$) |
| FITC-Dex 70k | 11 | 9.2 \pm 0.4 | 1.46 \pm 0.26 | 1.31 \pm 0.23 | 1.29 \pm 0.23 | 1.29 \pm 0.23 ($L_{p,\text{control}}=2\times 10^{-9}$) |

Values are mean \pm SE. N, number of vessels. Hydraulic conductivity L_p in cm/s/cmH₂O. Control $L_{p,\text{control}}$ is from Kimura et al. (1993).